Polymer Chemistry

PAPER
Kei Suzuki *et al.*
Effect of alkyl side chain length on microscopic structures
and mechanical properties of ionically-functionalized block
polymer-based thermoplastic elastomers

ROYAL SOCIETY
OF **CHEMISTRY**

15 YEARS
ANNIVERSARY

PAPER

Check for updates

Effect of alkyl side chain length on microscopic structures and mechanical properties of ionically-functionalized block polymer-based thermoplastic elastomers†

Kei Suzuki,[a] Takato Kajita, [ID] [a] Mako Ota,[a] Yuki Nakama, [ID] [b] Yuki Tamura,[b] Saki Kinoshita, [ID] [b] Daisuke Kato, [ID] [b] Ryoji Oda,[b] Sadaharu Hashimoto[b] and Atsushi Noro [ID] *[a,c,d]

Recently, the demand for thermoplastic elastomers (TPEs) with high tensile strength and toughness has grown. In this study, we synthesized ionically-functionalized polystyrene-*b*-polyisoprene-*b*-polystyrene (i-SIS(n)) containing 7.1 mol% of monosodium succinate mono-alkyl amide units in the middle I block of SIS and investigated the effects of the alkyl side chain length on the formation of microscopic ionic aggregates and the mechanical properties, where n represents the carbon number of the alkyl side chains. Both neat SIS and i-SIS(n) formed cylindrical structures, while the microscopic structures in i-SIS(n) exhibited slightly smaller domain spacing and poor orientation of domains compared to those in neat SIS. Furthermore, i-SIS(n) formed microscopic ionic aggregates, and the core dimensions of these aggregates increased as the alkyl side chain length shortened. The relaxation behavior of i-SIS(n) was associated with the disassembly/re-assembly of the ionic aggregates. The time scale of this relaxation behavior tended to be longer for i-SIS(n) with the shorter alkyl side chains, suggesting that the ionic aggregates in i-SIS(n) with shorter alkyl side chains were stronger than those in i-SIS(n) with longer alkyl side chains. These results were attributed to the easier approach among ion pairs, facilitated by the reduced steric hindrance associated with the shorter alkyl chain length. Moreover, the ionic aggregates acted as physical cross-links, leading to superior tensile properties of i-SIS(n) compared to neat SIS. Additionally, the shorter alkyl side chains contributed to greater toughness as compared to the longer alkyl side chains.

1. Introduction

The recent syntheses of multi-component polymers prepared by combining different polymers at the molecular level have met a diverse range of needs. A block polymer is a type of multi-component polymer that consists of two or more polymers covalently bonded together.[1,2] In particular, ABA triblock copolymers composed of a glassy polymer A with a glass transition temperature (T_g) higher than room temperature and a molten polymer B with a T_g lower than room temperature exhibit high stretchability at room temperature.[3,4] This stretchability arises because the ABA triblock copolymers form a polymer network, with the soft middle B chains bridging between the isolated hard domains consisting of the terminal A chains. Thus, the ABA triblock copolymers behave as elastomers at room temperature. The entire block polymer melts when heated above a T_g of the hard A segment. Consequently, block polymer-based elastomers exhibit excellent processability and are referred to as thermoplastic elastomers (TPEs).

Typical block polymer-based TPEs include styrenic TPEs (TPSs) such as polystyrene-*b*-polybutadiene-*b*-polystyrene (SBS) and polystyrene-*b*-polyisoprene-*b*-polystyrene (SIS) triblock copolymers.[5–9] The development of SBS and SIS began with the discovery of living anionic polymerization by Szwarc and coworkers.[10,11] SBS became commercially available as Kraton through Shell Chemicals.[12,13] Demand for TPSs, which exhibits rubber elasticity without vulcanization and offers excellent processability, continues to grow as a cost-effective alternative to vulcanized rubbers.[14] For instance, in automotive appli-

[a]Department of Molecular & Macromolecular Chemistry, Graduate School of Engineering, Nagoya University, Furo-cho, Chikusa-ku, Nagoya 464-8603, Japan. E-mail: noro@nagoya-u.jp
[b]Zeon Corporation, 1-6-2 Marunouchi, Chiyoda-ku, Tokyo 100-8246, Japan
[c]Institute of Materials Innovation, Institutes of Innovation for Future Society, Nagoya University, Furo-cho, Chikusa-ku, Nagoya 464-8601, Japan
[d]Research Center for Net-Zero Carbon Society, Institutes of Innovation for Future Society, Nagoya University, Furo-cho, Chikusa-ku, Nagoya 464-8601, Japan
†Electronic supplementary information (ESI) available: GPC chromatograms of neat SIS and s-SIS; ^{1}H NMR spectrum of neat SIS; FT-IR spectra of h-SIS(n) and i-SIS(n). See DOI: https://doi.org/10.1039/d5py00109a

cations, TPS is used in weatherstripping for window frames, instrument panels for control systems, and insulation for hoses and wires within the engine compartment.

In recent years, as the applications of TPEs have expanded, demand has grown for tough TPEs with high tensile strength and toughness, which is an indicator of resistance to material breakage. To enhance the toughness of block polymer-based TPEs, researchers have attempted to introduce noncovalent interactions, such as hydrogen bonding,[15–26] metal–ligand coordination,[27–33] ionic interactions,[34–41] host–guest interactions,[42–44] and others into the polymer chain. Weiss and coworkers synthesized block polymer-based TPEs with ionic groups in the hard A terminal chains by sulfonating the polystyrene blocks in a triblock copolymer.[45] Long and co-workers reported ABA triblock copolymer-based TPEs with hydrogen bonding groups in the A terminal chain.[46] On the other hand, in 2015, we synthesized poly(4-vinylpyridine)-*b*-poly(*n*-butyl acrylate-*co*-acrylamide)-*b*-poly(4-vinylpyridine), by incorporating hydrogen-bonding groups in the middle block chain that behaves as a soft segment at room temperature.[47,48] Yoshie and coworkers also reported ABA triblock copolymer-based TPEs composed of norbornene backbones with hydrogen-bonding groups.[49] Additionally, Robertson and a coworker have prepared styrenic ABA triblock copolymers with hydrogen-bonding groups in the acrylate middle block.[50]

We have also developed ionically-functionalized SIS (i-SIS) containing ionic monosodium succinate mono-*n*-butyl amide units in the middle I block.[51–53] With metal alkoxide, the i-SIS was synthesized by neutralizing hydrogen-bonded SIS (h-SIS) containing succinic acid mono-*n*-butyl amide units. The h-SIS was synthesized by reacting normal butylamine with succinic anhydride-incorporated SIS (s-SIS), which was synthesized by introducing succinic anhydride units into the I block of SIS. In the i-SIS films, microscopic ionic aggregates were formed due to ionic interactions between carboxylate anions and metal cations.[54,55] These ionic aggregates acted as transient physical cross-linking domains, increasing the apparent cross-link density and resulting in higher stress.[56] Meanwhile, the reversible disassembly and re-assembly of the ionic aggregates during elongation can dissipate the stress applied on the polystyrene hard domains, thereby maintaining high strain capability. Consequently, i-SIS exhibited excellent toughness. Furthermore, i-SIS containing specific types of metal cations exhibited higher impact resistance than glass fiber reinforced plastics (GFRPs), which are typical high-strength materials. In addition, we reported that peel strength and impact resistance of cured adhesives were enhanced by mixing an epoxy resin with h-SIS, compared to an adhesive without h-SIS.[57]

In the monosodium succinate mono-*n*-butyl amide unit in the i-SIS, the alkyl group positioned near the sodium carboxylate ion pair could introduce steric hindrance and affect the ability of the sodium carboxylate ion pairs to interact. A shorter alkyl chain could reduce steric hindrance, allowing the ion pairs to more easily approach each other and to form microscopic ionic aggregates composed of the ion pairs (Fig. 1). Consequently, i-SIS with a shorter alkyl chain in the
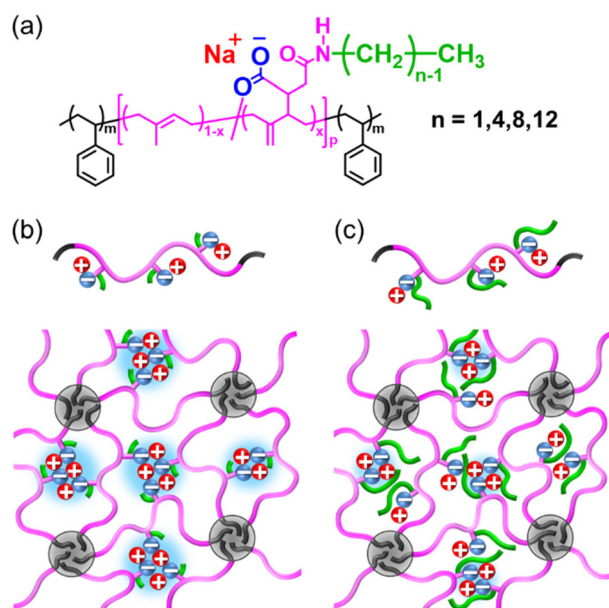
Fig. 1 (a) Chemical structure of i-SIS(*n*) and schematic molecular-level illustrations of i-SIS with (b) short, and (c) long normal alkyl side chains around ionic groups. The black short lines, pink curved lines, and green short lines represent polystyrene, polyisoprene, and normal alkyl side chains, respectively. The small blue and red spheres represent carboxylate anion and sodium cation, respectively. The regions composed of the black short lines depict isolated glassy polystyrene domains, while the blurred light blue spheres illustrate ionic aggregates.

monosodium succinate mono alkyl amide unit is expected to exhibit superior mechanical properties compared to i-SIS with a longer alkyl chain. However, the effects of the length of the alkyl side chain on the mechanical properties have not been evaluated, despite the importance of such an evaluation in controlling the mechanical properties of i-SIS.

In this study, we have synthesized i-SIS with alkyl side chains of varying lengths around the ionic groups (i-SIS(*n*)), where *n* represents the carbon number of the alkyl side chains (*n* = 1, 4, 8, and 12). The i-SIS is synthesized by reacting s-SIS with normal alkylamines of different carbon numbers to convert succinic anhydride units into succinic acid mono alkyl amide units, followed by neutralization with a metal alkoxide. The effects of alkyl side chain length in the i-SIS(*n*) on the formation of microscopic ion aggregates and mechanical properties are investigated.

2. Experimental

2.1 Materials

Neat SIS was synthesized *via* sequential living anionic polymerization, followed by purification through reprecipitation. The number-average molecular weight (M_n) and dispersity (M_w/M_n) of neat SIS were determined to be 175k and 1.12, respectively, by gel permeation chromatography (Fig. S1†), which was calibrated with polystyrene standards. The weight fraction of poly-

styrene of neat SIS was determined to be 19 wt% by ^{1}H NMR. Maleic anhydride, normal butylamine, normal octylamine, and normal dodecylamine were purchased from TCI. A 2 mol L^{-1} tetrahydrofuran (THF) solution of methylamine was supplied from Sigma-Aldrich. Sodium methoxide in methanol (*ca.* 5 mol L^{-1}) was also supplied from TCI. Irgafos 168 and Irganox 565 used as antioxidants were purchased from BASF.

2.2 Synthesis of ionically functionalized SIS

Scheme 1 shows synthetic scheme of i-SIS. The s-SIS was synthesized according to our previous report,[51,52,57] where the molar fraction of succinic anhydride units in the polyisoprene block of s-SIS was 7.1 mol% (see also the GPC chromatogram of s-SIS in Fig. S1†). A typical synthetic procedure for synthesizing h-SIS is as follows: s-SIS (approximately 4 g) was dissolved in dried tetrahydrofuran (THF) (40 mL) under an argon gas atmosphere. A normal alkylamine (methylamine, butylamine, octylamine, or dodecylamine) (3–4 molar equivalents per succinic anhydride unit in s-SIS) was added to the solution, and the mixture was stirred at 50 °C for 24 h. The product was then reprecipitated using acetonitrile to yield succinic acid monoalkyl amide unit-incorporated SIS, designated as h-SIS(*n*), where *n* represents the carbon number of the normal alkylamine used, *i.e.*, the carbon number of the alkyl group attached to the nitrogen atom of the amide group in h-SIS.

Finally, ionically-functionalized SIS, i-SIS(*n*), was synthesized by neutralizing carboxy acid groups in h-SIS(*n*) with sodium methoxide, following our previous report.[51,52] i-SIS(*n*) films were prepared by a solution-casting method using a mixed solvent of THF/methanol (9/1, wt/wt) with antioxidants at 40 °C for 2 days, followed by vacuum drying at 40 °C for 2 days.

2.3 Characterizations

GPC measurements were carried out using an HPLC system (HPLC pump: Shimadzu LC-20 AD; column oven: Shimadzu CTO-20A; refractive index (RI) detector: RID-20A; column: two TSKgel GMH$_{HR}$-M columns [Tosoh]) to determine the M_n and M_w/M_n of neat SIS and s-SIS, and to confirm whether any side reactions, such as multimer formation or decomposition, occurred during synthesis of s-SIS. The eluent solvent was THF, and molecular weights were calibrated with polystyrene standards.

^{1}H NMR spectra were recorded using an AVANCE III HD 500 MHz NMR spectrometer (Bruker) to estimate the fraction of succinic anhydride and alkylamide units. Deuterated chloroform was used as a solvent.

Fourier transform infrared (FT-IR) spectroscopy of neat SIS, s-SIS, h-SIS(*n*), and i-SIS(*n*) was performed using an FT/IR-6100 spectrometer (JASCO) at ambient temperature. Samples were prepared on a potassium bromide plate using the drop-casting method.

Differential scanning calorimetry (DSC) was performed using a Q2000 calorimeter (TA Instruments) to determine glass transition temperatures (T_gs) of i-SIS(*n*). Measurements were carried out over a temperature range from −70 to 125 °C at a heating rate of 10 °C min^{-1}, under a nitrogen gas flow rate of 50 mL min^{-1}.

2.4 Measurements

Transmission electron microscopy (TEM) observation was carried out to observe the nanostructures of the i-SIS(*n*) films using an HT7700 electron microscope (Hitachi) operated at an acceleration voltage of 100 kV. Ultrathin sections of samples were prepared by embedding sample films in an epoxy resin, followed by sectioning using a cryo-microtome method. The sections were stained with osmium tetroxide (OsO$_4$) vapor for enhanced contrast.[6,58,59]

Small-angle X-ray scattering (SAXS) measurements were also conducted using a NANOPIX diffractometer (Rigaku) to evaluate the microscopic structure of the i-SIS(*n*) films. The wavelength of the X-ray was 0.154 nm, and the camera length was set to 1344 mm.[58,59] To determine the dimension of ionic aggregates in the i-SIS(*n*) films, we assumed that spherical ionic aggregates were randomly dispersed and simulated the SAXS patterns using the Yarusso–Cooper model[60,61] expressed by the following equations:
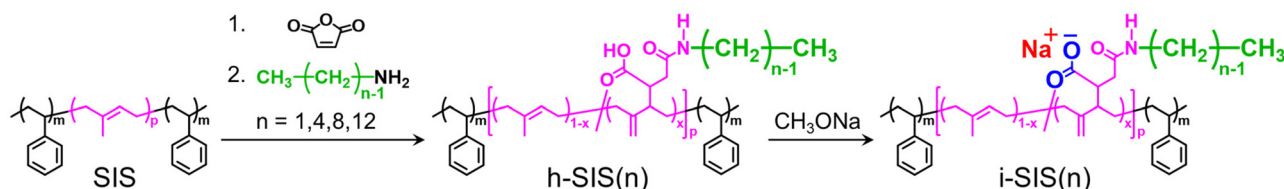
$$I(q) = \frac{A}{v_p} v_1{}^2 \Phi^2(qR_1) \frac{1}{1 + \frac{8v_{CA}}{v_p}\Phi(2qR_{CA})} \quad (1)$$

$$v_1 = \frac{4}{3}\pi R_1{}^3 \quad (2)$$

$$v_{CA} = \frac{4}{3}\pi R_{CA}{}^3 \quad (3)$$

$$\Phi(x) = 3\frac{\sin x - x \cos x}{x^3} \quad (4)$$

where A, v_p, R_1, and $2R_{CA}$ are a constant, the average sample volume occupied by one particle of the ionic core, the radius of the electron dense ionic core, and the closest approach dis-

Scheme 1 Synthesis of i-SIS(*n*).

tance between two aggregates composed of the ionic core and the hydrocarbon shell, respectively.[60–62] In this study, curve fitting was performed using the relative scattering intensity ($I_{rel}(q)$). When the fitting was performed on $I_{rel}(q)$, rather than on the absolute intensity ($I(q)$), the shape of the SAXS pattern is determined by three parameters (R_1, R_{CA}, and v_p). The coefficient Av_1^2/v_p is treated as an adjustable parameter for intensity scale. Therefore, the A value itself does not carry physical meaning in this context.[62]

To investigate the dynamic mechanical behavior of i-SIS(n), dynamic mechanical shear measurements were performed using an ARES-G2 shear rheometer (TA Instruments) equipped with 8 mm diameter parallel plates. The measurements were conducted within an angular frequency (ω) range from 4.0×10^2 to 1.0×10^{-3} s^{-1} at ambient temperature. Temperature ramp tests were also performed from −50 to 130 °C at a heating rate of 2 °C min^{-1} under a 1% strain at an ω of 1 s^{-1}.

Tensile tests were also carried out at ambient temperature with an approximately 10 mm initial specimen distance between jigs using an AGS-X mechanical tester (Shimadzu) to evaluate the mechanical properties of i-SIS(n). The elongation rate was set at approximately 1.0 mm s^{-1}, corresponding to an initial strain rate ($\dot{\varepsilon}_0$) of 0.10 s^{-1}.[36,51,52] Test specimens with a thickness of approximately 0.90 mm were prepared by punching the solution-casting films with a die conforming to the standards of ISO 37:2017 Type 4 (JISK 6251:2017 Dumb-bell Type 7). Tests were conducted at least three times for each sample.

3. Results and discussion

3.1 Characterizations of h-SIS(n) and i-SIS(n)

3.1.1 NMR measurements. Using ^{1}H NMR spectroscopy, we estimated the incorporation fraction of functional groups in h-SIS(n) and its precursor, s-SIS. Fig. 2 shows the ^{1}H NMR spectra of s-SIS, h-SIS(1), h-SIS(4), h-SIS(8), and h-SIS(12), along with the partial chemical structures present in the polymers (see also the ^{1}H NMR spectrum of neat SIS in Fig. S2†). The mole fraction of the succinic anhydride unit attached to the I block in s-SIS was estimated to be 7.1 mol%, based on the integral ratio of the peak at 4.5–5.4 ppm, originating from the protons on the double bonds of the polyisoprene unit (d and e), and the peak at 2.3–3.5 ppm, originating from the three protons (h′ and i′) on the succinic anhydride unit and the one proton (g′) on the carbon atom adjacent to the succinic anhydride unit. In the spectrum of h-SIS(1), the peaks originating from the g′–i′ protons in the spectrum of s-SIS shifted due to the reaction of the succinic anhydride unit with methylamine. The progress of the acyl substitution reaction between the succinic anhydride unit and methylamine was estimated to be 94% conversion. This value was determined by comparing the integral ratio of the peaks originating from the g′–i′ protons with the integral ratio of the peaks at 2.3–3.2 ppm originating from the protons on the methine group (h), methylene group (i), and methyl group adjacent to the nitro-
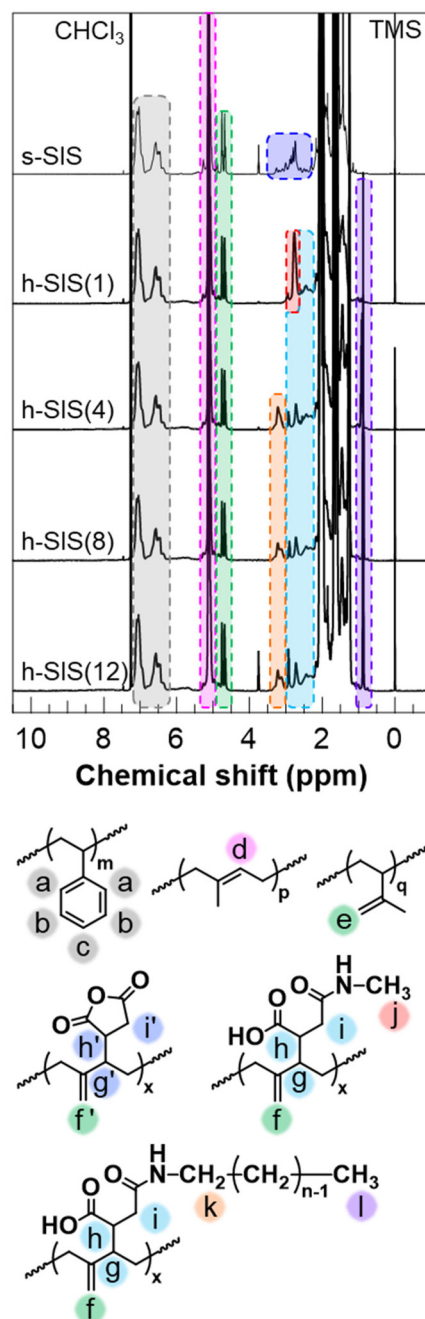

Fig. 2 ^{1}H NMR spectra of s-SIS, h-SIS(1), h-SIS(4), h-SIS(8) and h-SIS(12), and chemical structures of polystyrene, poly(1,4-isoprene), poly(3,4-isoprene), succinic anhydride incorporated-poly(1,4-isoprene), and hydrogen bonding group-incorporated poly(1,4-isoprene), where chemical structures of other isomers are omitted for simplicity.

gen atom (j), and the methine group (g) to which the succinic acid monomethyl amide unit (−CH(COOH)−CH$_2$−CONH−CH$_3$) was attached.

^{1}H NMR spectroscopy for h-SIS(4) revealed the peaks derived from the g′–i′ protons in the spectrum of s-SIS shifted due to the reaction of the succinic anhydride unit with normal butylamine, similar to changes observed in h-SIS(1). On the

other hand, the chemical shift of the peak originating from the succinic acid mono alkyl amide unit differed from that of h-SIS(1) since the nitrogen atom in the amide group was adjacent to a methylene group instead of a methyl group. Namely, peaks originating from the protons on the methine group of the succinic acid mono-*n*-butyl amide unit (h), the methylene group adjacent to the carbonyl group (i), and the methine group (g) adjacent to the succinic acid mono-*n*-butyl amide unit appeared at 2.3–3.0 ppm. Peaks originating from the protons on the methylene group adjacent to the nitrogen atom of the succinic acid mono-*n*-butyl amide unit (k) appeared at 3.0–3.5 ppm, while a peak originating from the protons on the methyl group of the succinic acid mono-*n*-butyl amide unit (l) appeared at 0.8–1.0 ppm. A comparison of the integral ratio of the peaks originating from the g′–i′ protons with that of the peaks originating from k protons revealed that the acyl substitution reaction between the succinic anhydride unit and *n*-butylamine progressed to over 99% conversion. The ^{1}H NMR spectra of h-SIS(8) and h-SIS(12) were similar to that of h-SIS (4). The acyl substitution reaction between the succinic anhydride unit and the normal alkylamine progressed to 96% conversion and over 99% for h-SIS(8) and h-SIS(12), respectively, based on estimations performed in the same manner as for h-SIS(4). In summary, more than 90% conversion of the succinic anhydride units to amide unites were found in all h-SIS(n).

3.1.2 FT-IR measurements. FT-IR spectroscopy was also performed on neat SIS, s-SIS, h-SIS(1), and i-SIS(1) to confirm the presence of hydrogen bonds and the progress of the reaction. We measured the FT-IR spectra in the range of 1500–2000 cm^{-1} (Fig. 3a), where absorption bands mainly attributed to the stretching vibration of the carbonyl group (C=O) appeared. We also measured the spectra in the range of 3100–3600 cm^{-1} (Fig. 3b), where absorption bands primarily derived from the stretching vibrations of the N–H in the amide group and the O–H in the carboxyl group appeared. Absorptions derived from the stretching vibration of C=O in the succinic anhydride unit appeared at 1790 and 1864 cm^{-1} in the s-SIS spectrum. In contrast, these absorptions disappeared in the h-SIS(1) spectrum, where new absorptions appeared around 1710–1730 cm^{-1} and 1640 cm^{-1}, corresponding to the C=O stretching vibrations of the carboxyl group and amide group, respectively.[16,39,51,63,64] In addition, the spectrum of h-SIS(1) showed broad absorption bands at approximately 3230–3470 cm^{-1}, corresponding to the O–H stretching vibration of the hydrogen-bonded carboxyl group and the N–H stretching vibration of the hydrogen-bonded amide group. These absorption bands were not observed in the s-SIS spectrum. The results indicated that the succinic anhydride unit in s-SIS reacted with methylamine to form a carboxyl group and an amide group in h-SIS(1). Additionally, the FT-IR spectra in Fig. S3† revealed that other h-SIS(n) had absorptions derived from carboxyl and amide groups, similar to h-SIS(1).

In the FT-IR spectrum of i-SIS(1), the absorption band at 1710–1730 cm^{-1} nearly disappeared, while a new absorption
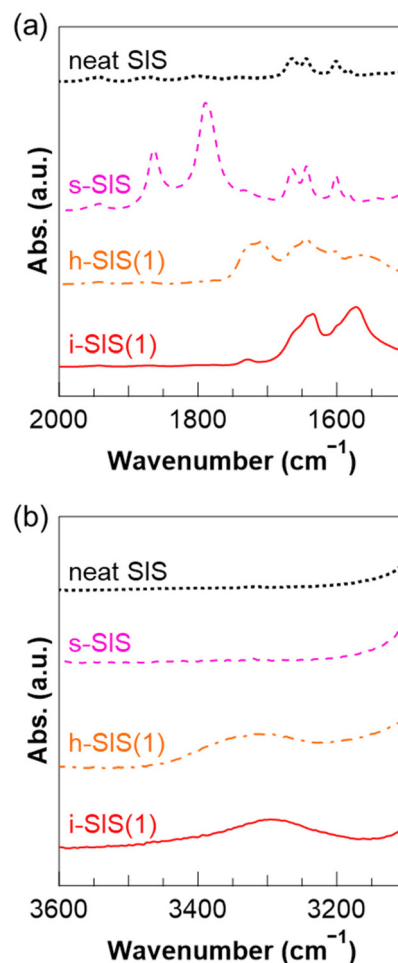
Fig. 3 FT-IR spectra of neat SIS (black dotted line), s-SIS (pink dashed line), h-SIS(1) (orange dashed-dotted line), and i-SIS(1) (red solid line) within the wavenumber ranges of (a) 1500 to 2000 cm^{-1} and (b) 3100 to 3600 cm^{-1}.

band corresponding to the stretching vibration of the ionic carboxylate group appeared around 1570 cm^{-1}.[39,51] In addition, the absorption bands around 3230–3470 cm^{-1} observed in the spectrum of h-SIS(1) slightly shifted to approximately 3170–3500 cm^{-1}, indicating the conversion of the carboxy group to the ionic carboxylate group and the successful synthesis of i-SIS(1). The changes in the absorption are due to the conversion of carboxy groups to ionic carboxylate groups in i-SIS(1), confirming the successful synthesis of i-SIS(1). As shown by the FT-IR spectra in Fig. S3,† the other i-SIS(n) also contained the carboxylate groups converted from the carboxy groups in the h-SIS(n).

3.1.3 DSC measurements. DSC measurements were carried out to examine the effect of alkyl side chain length on the T_g of the middle block in i-SIS(n). Fig. 4 presents DSC thermograms of neat SIS, i-SIS(1), i-SIS(4), i-SIS(8), and i-SIS(12). Table 1 summarizes the T_g of the middle I block for each polymer, as determined by the DSC measurements. It should be noted that the T_g of the S block was not clearly observed in
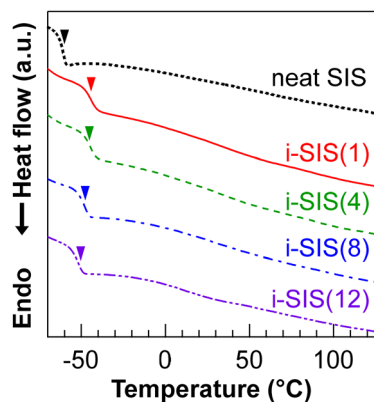
Fig. 4 DSC thermograms of neat SIS (black dotted line), i-SIS(1) (red solid line), i-SIS(4) (green dashed line), i-SIS(8) (blue dashed-dotted line), and i-SIS(12) (purple dashed-two-dotted line). Arrows indicate the positions of T_g of the middle block.

the DSC measurements, probably due to the small volume fraction of the S block.[22,65,66] The T_g of the I block in neat SIS was -61 °C, while the T_g values of the ionically-functionalized I (i-I) block in i-SIS(n) ranged from -50 to -44 °C. Thus, the i-I block in the i-SIS(n) exhibited a slightly higher T_g compared to the I block in neat SIS. This result suggests that the ionic interactions in the i-I block of i-SIS(n) slightly restricted the segmental motions of the polymer chains. A comparison of the i-SIS samples with different alkyl side chain lengths showed that the T_g of i-SIS(n) with a shorter alkyl side chain was slightly higher than that of i-SIS(n) with a longer alkyl side chain. The higher steric hindrance originating from the longer alkyl side chain probably masked the ionic interactions, resulting in reduced restriction of the segmental motions of the middle polymer chains. Additionally, the longer alkyl chain probably behaves like a plasticizer. The middle block of i-SIS (n) consists of approximately 7 mol% functionalized isoprene monomer units and 93 mol% isoprene monomer units. As a result, the T_g is predominantly influenced by unmodified 93 mol% isoprene monomer units, and the effect of the alkyl chain length in the functionalized isoprene monomer units on the T_g is relatively small.

3.2 Nanostructures of i-SIS(n)

To investigate the effect of the alkyl side chain length in i-SIS (n) on the formation of phase-separated structures and microscopic ionic aggregates, we used TEM observation and SAXS measurements to analyze the nanostructures of neat SIS and i-SIS(n) films. In typical TEM images of neat SIS, i-SIS(1), i-SIS (4), i-SIS(8), and i-SIS(12) films, the polystyrene phase appears brighter while the polyisoprene and ionically-functionalized polyisoprene phases appear darker due to staining with OsO$_4$ (Fig. 5).[6,58,59] A cylindrical structure resulting from phase separation of the block polymer was observed in the TEM image of the neat SIS film, with a domain spacing of approximately 30–40 nm. Although orientation of domains in i-SIS(n) was poorer than that in the neat SIS film, we confirmed that all the i-SIS(n) films formed cylindrical structures with the domain spacings of approximately 30–40 nm, similar to those of the neat SIS film.

We compared the SAXS profiles of neat SIS, i-SIS(1), i-SIS(4), i-SIS(8), and i-SIS(12) films (Fig. 6). In the profile of neat SIS, the first-order peak (q_1) was found at the scattering vector ($q = 4\pi \sin \theta/\lambda$) of 0.18 nm^{-1}. Distinct peaks were also observed at relative q positions of approximately $3^{1/2}$, $4^{1/2}$, $7^{1/2}$, $9^{1/2}$, and $12^{1/2}$ with respect to q_1, indicating that the neat SIS film formed a cylindrical phase-separated structure. The domain spacing ($D = (4/3)^{1/2} \times 2\pi/q_1$) was estimated to be 41 nm based on the q_1 value (Table 1), which was roughly consistent with the D estimated from the TEM image. In the profiles of i-SIS (1), i-SIS(4), i-SIS(8), and i-SIS(12) films, q_1 was found at $q = 0.20$ nm^{-1}, which was slightly higher than that of neat SIS. Peaks were also found at relative q positions of approximately $3^{1/2}$, $4^{1/2}$, $7^{1/2}$, and $9^{1/2}$ with respect to q_1. However, the higher-order peaks were very broad, unlike those of neat SIS. These results indicate that the i-SIS(1), i-SIS(4), i-SIS(8), and i-SIS(12) films also formed cylindrical structures, with D values estimated to be $\sim$36 nm (Table 1), which is smaller than that of the neat SIS films. The smaller domain spacing of i-SIS than that of neat SIS was probably resulted from the formation of the ionic aggregates within the matrix of i-SIS(n). Accordingly, the difference in domain spacing between neat SIS and i-SIS(n) basically arises from a result of thermodynamic effects. Furthermore, the broad peaks also suggest that the orientation

Table 1 Properties of neat SIS and i-SIS(n)s

Sample	$T_g{}^a$ (°C)	D^b (nm)	$R_1{}^c$ (nm)	$R_{CA}{}^d$ (nm)	$\nu_p{}^e$ (nm^3)	$E_Y{}^{f,g}$ (MPa)	$\sigma_{max}{}^{f,h}$ (MPa)	$\varepsilon_b{}^{f,i}$ (−)	$W_T{}^{f,j}$ (MJ m^{-3})
Neat SIS	-61	41	—	—	—	3.5 ± 0.1	9.0 ± 0.1	30 ± 0.2	130 ± 2
i-SIS(1)	-44	36	1.1 ± 0.002	2.2 ± 0.0008	71 ± 0.1	32 ± 1.2	33 ± 1.5	16 ± 0.3	320 ± 20
i-SIS(4)	-45	36	0.87 ± 0.002	1.9 ± 0.002	68 ± 0.2	27 ± 0.9	31 ± 1.1	17 ± 0.6	300 ± 19
i-SIS(8)	-48	36	0.79 ± 0.005	1.7 ± 0.002	52 ± 0.3	15 ± 0.8	23 ± 3.5	18 ± 2.2	240 ± 60
i-SIS(12)	-50	36	0.73 ± 0.02	1.5 ± 0.006	36 ± 0.6	8.3 ± 0.3	14 ± 0.3	19 ± 1.0	150 ± 9

^{a} Glass transition temperature of the middle block. ^{b} Domain spacing estimated from SAXS profiles. ^{c} Radius of the ionic core in the ionic aggregate determined by the Yarusso–Cooper model. ^{d} Radius of the ionic aggregate, composed of the ionic core and the hydrocarbon shell, determined by the Yarusso–Cooper model. ^{e} Average sample volume occupied by one ionic core. ^{f} Average value estimated by measuring at least three test specimens of the same sample, with the standard error of the mean provided for at least three measurements. ^{g} Young's modulus, estimated from the slope within a tensile strain range from 0 to 10%. ^{h} Tensile strength. ^{i} Elongation at break. ^{j} Tensile toughness, estimated from the inner area of the stress–strain curve.
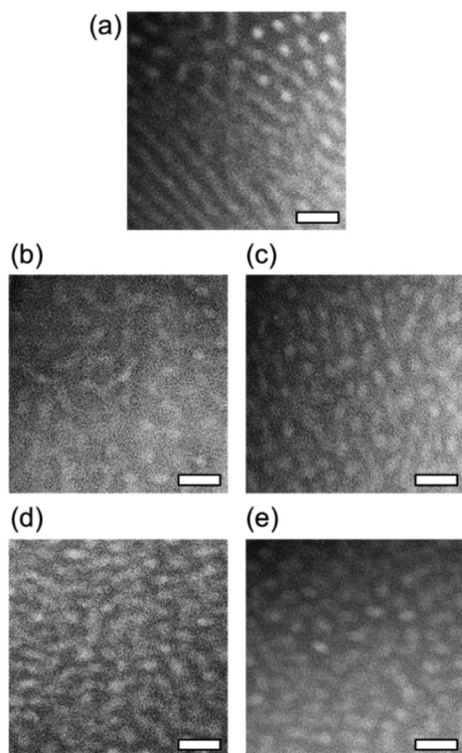
Paper

Fig. 5 TEM images of (a) neat SIS, (b) i-SIS(1), (c) i-SIS(4), (d) i-SIS(8), and (e) i-SIS(12).
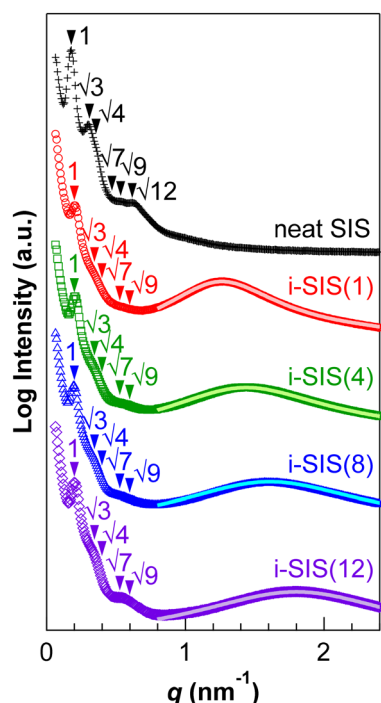

Fig. 6 SAXS profiles of neat SIS (black plus marks), i-SIS(1) (red open circles), i-SIS(4) (green open squares), i-SIS(8) (blue open triangles), and i-SIS(12) (purple open diamonds). The light-colored solid lines over the profiles of i-SIS(n) represent fitting curves based on the Yarusso–Cooper model.

of the cylindrical domains in i-SIS(n) was less pronounced compared to that in neat SIS. These findings roughly agreed with the results of TEM observations. It is indeed possible that annealing at a temperature higher than order–disorder transition (ODT) leads to better structural organization.

Meanwhile, the SAXS profiles of i-SIS(1), i-SIS(4), i-SIS(8), and i-SIS(12) films showed a broad peak at $q > 1$ nm^{-1}, which was not found in the SAXS profile of neat SIS (Fig. 6). This scattering peak originates from microscopic ionic aggregates. These ionic aggregates may have restricted molecular motions during the preparation of the i-SIS(n) films, probably contributing to the difference in the D value and the orientation of the cylindrical structures between neat SIS and i-SIS(n). We also performed curve fitting using the Yarusso and Cooper's model[60,61] represented by eqn (1)–(4) for the peaks originating from the ionic aggregates. The fitting curves are shown in Fig. 6 and the fitting parameters are summarized in Table 1. The radius of the ionic core in the ionic aggregate (R_1) decreased as the alkyl side chain length increased; specifically, R_1 of i-SIS(1) was 1.1 nm, while that of i-SIS(12) was 0.73 nm. The radius of the ionic aggregate composed of the ionic core and the hydrocarbon shell (R_{CA}) as well as the average sample volume occupied by one ionic core (v_p) also decreased as the alkyl side chain length increased, where the reciprocal of v_p corresponds to the number density of ionic aggregates in the samples. According to Table 1, the number density of ionic aggregates in i-SIS(n) with shorter alkyl side chains was lower than that in i-SIS(n) with longer alkyl side chains. The larger dimensions of the ionic aggregates in i-SIS(n) with shorter alkyl side chains resulted from the easier approach of ion pairs, facilitated by the reduced steric hindrance associated with the shorter alkyl chain length.

3.3 Dynamic mechanical properties of i-SIS(n)

Dynamic mechanical measurements were carried out to investigate the effect of alkyl side chain length on the mechanical properties of i-SIS(n). These measurements afforded information for the storage moduli (G'), loss moduli (G'') and tan δ (=G''/G') acquired by dynamic frequency sweep tests for neat SIS and i-SIS(n) films at room temperature (Fig. 7). G' of neat SIS was nearly constant at ~0.8 MPa over the frequency range of 1.0×10^{-3}–4.0×10^2 s^{-1}, whereas G' of all i-SIS(n) samples varied with frequency, being higher at higher frequencies. Notably, G' of i-SIS(n) exceeded that of neat SIS above 10^0 s^{-1}. This result was attributed to the higher apparent cross-link density of i-SIS(n), caused by the formation of the microscopic ionic aggregates. We observed almost identical G' curves for i-SIS(n), i-SIS(1), and i-SIS(4) with shorter alkyl side chains. In contrast, G' of i-SIS(8) with longer alkyl side chains was lower than that of i-SIS(1) and that of i-SIS(4). Furthermore, i-SIS(12) showed an even lower G' than i-SIS(8). The smaller dimensions of the ionic aggregates in i-SIS(n) with the longer alkyl side chains resulted in the lower G' observed for i-SIS(n) with the longer alkyl side chains. In addition, the G' values of i-SIS(8) and i-SIS(12) were lower than that of neat SIS at the low frequencies, likely because the ionic aggregates contributed mini-
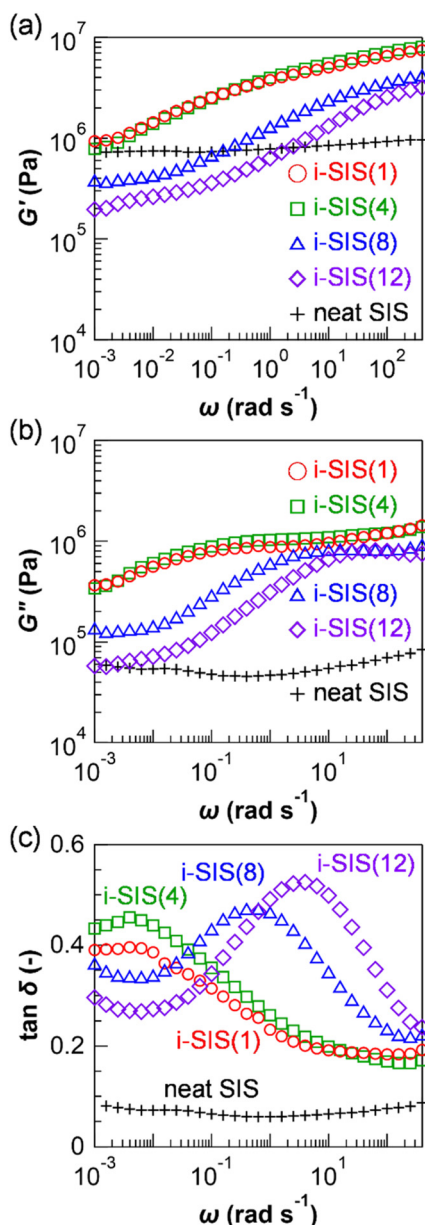
Fig. 7 Frequency dependence of (a) storage moduli, G', (b) loss moduli, G'', and (c) tan δ acquired by dynamic mechanical tests at room temperature for neat SIS (black plus marks), i-SIS(1) (red open circles), i-SIS(4) (green open squares), i-SIS(8) (blue open triangles), and i-SIS(12) (purple open diamonds).

mally as physical cross-links in the low frequency region where the ionic aggregates were fully relaxed, while the longer alkyl side chains may have acted as plasticizers across all frequency range.

We observed no peaks in the tan δ curves of neat SIS. However, a peak derived from relaxation modes associated with the association and dissociation of the ionic aggregates appeared in the tan δ curves of i-SIS(n). The tan δ curve of i-SIS (1) with a short alkyl side chain displayed a peak with a tan δ value of 0.40 at 4.0×10^{-3} s^{-1}. The tan δ curve of i-SIS(4) also

had a peak at 4.0×10^{-3} s^{-1}, with a tan δ peak of 0.46, which was slightly higher than that of i-SIS(1). This outcome suggests that the relaxation mode originating from the ionic aggregates in i-SIS(1) and i-SIS(4) arose on almost the same time scale, while the stress dissipation capability associated with the relaxation mode was slightly higher in i-SIS(4) than in i-SIS(1). In the tan δ curve of i-SIS(8) with a long alkyl side chain, we observed a peak with tan δ = 0.47 at a higher frequency of 6.3×10^{-1} s^{-1} compared to those of i-SIS(1) and i-SIS(4). Additionally, a peak with tan δ = 0.53 appeared at an even higher frequency of 4.0×10^{0} s^{-1} in the tan δ curve of i-SIS(12) compared to that of i-SIS(8). These results indicate that the relaxation mode originating from the ionic aggregates in i-SIS (n) with the longer alkyl side chains is observed on a faster time scale than in i-SIS(n) with the shorter alkyl side chain. The fast relaxation observed in i-SIS(n) with the longer alkyl side chain may reflect the reduced ability of ion pairs to approach each other, caused by the higher steric hindrance of the longer alkyl side chains.

To evaluate the temperature dependence of the dynamic mechanical properties of i-SIS(n), we also performed the dynamic mechanical measurements with a temperature ramp at 1 s^{-1} (Fig. 8). The G' curve of neat SIS exhibited a glass transition region from −50 to −40 °C, which originates from the T_g of the I block, and a constant rubbery plateau with G' of ~0.8 MPa in the range of −40 to 80 °C. Above 80 °C, G' of neat SIS decreased due to the T_g of the S block. Namely, neat SIS exhibited the typical viscoelastic behavior of TPEs. On the other hand, in the tan δ curve of i-SIS(1), a peak with a tan δ value of 0.39 was observed around 56 °C, attributed to the relaxation mode associated with the association and disassembly of ionic aggregates in the ionically-functionalized I (i-I) block. Additionally, the G' value in the temperature range below 56 °C was several times higher than the plateau value of neat SIS. i-SIS(4) also exhibited dynamic viscoelastic behavior similar to that of i-SIS(1). However, the tan δ peak value, attributed to the relaxation mode of the association and dissociation of the ionic aggregates in i-SIS(4), was 0.44, which was higher than that of i-SIS(1). This result was similar to the trend seen in the dynamic frequency sweep tests shown in Fig. 7. In the tan δ curves of i-SIS(8) and i-SIS(12) with the longer alkyl side chains, tan δ peaks appeared at 26 °C and 18 °C, respectively, indicating that the relaxation mode originating from the ionic aggregates assembly/disassembly in i-SIS(8) and i-SIS(12) is observed at lower temperatures than those in i-SIS(1) and i-SIS (4). This observation is consistent with the results acquired by the dynamic frequency sweep tests as shown in Fig. 7. The relaxation behavior at the lower temperatures in i-SIS(n) with longer alkyl side chain was also attributed to the reduced ability of ion pairs to approach each other, caused by the higher steric hindrance of the longer alkyl side chains. Furthermore, the G' values of i-SIS(8) and i-SIS(12) were lower than that of neat SIS above 30 °C or 40 °C, respectively, probably because the ionic aggregates contributed minimally as physical cross-links in the lower temperature region where the ionic aggregates were fully relaxed, and the longer alkyl side
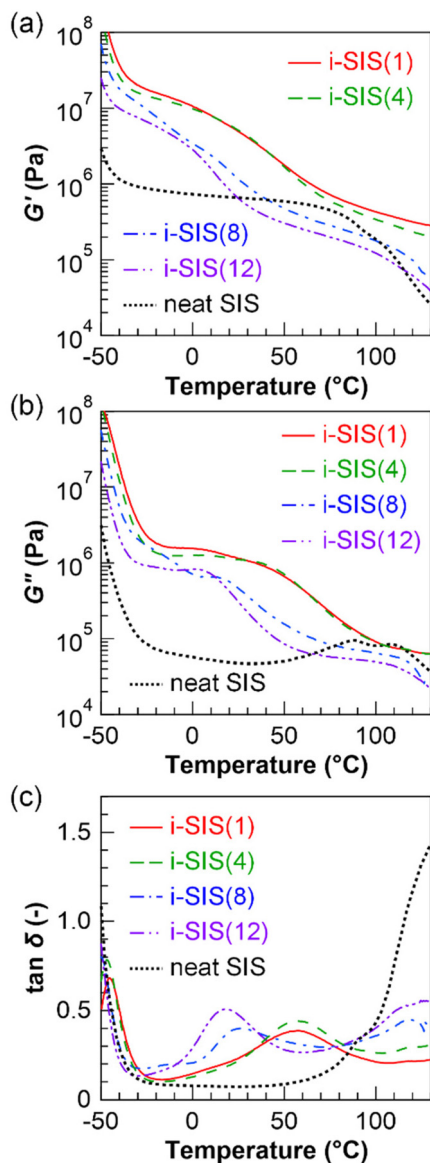
Fig. 8 Temperature dependence of (a) G', (b) G'', and (c) tan δ acquired by dynamic mechanical tests for neat SIS (black dotted line), i-SIS(1) (red solid line), i-SIS(4) (green dashed line), i-SIS(8) (blue dashed-dotted line), and i-SIS(12) (purple dashed-two-dotted line).

Fig. 9 Typical tensile stress–strain curves of neat SIS (black dotted line), i-SIS(1) (red solid line), i-SIS(4) (green dashed line), i-SIS(8) (blue dashed-dotted line), and i-SIS(12) (purple dashed-two-dotted line).

chains may have acted as plasticizers in all temperature range. These results are also consistent with the results acquired by the dynamic frequency sweep tests shown in Fig. 7.

3.4 Tensile properties of i-SIS(n)

We evaluated the tensile properties of the neat SIS and i-SIS(n) films including stress–strain curves (Fig. 9) and related parameters derived from these curves (Table 1). These values were obtained from at least three measurements, where the average values and standard errors of Young's modulus (E_Y) and tensile toughness (W_T) were estimated from the slope of the stress–strain curve within the strain range of 0–10% and the inner area under the stress–strain curve (Fig. 9), respectively.
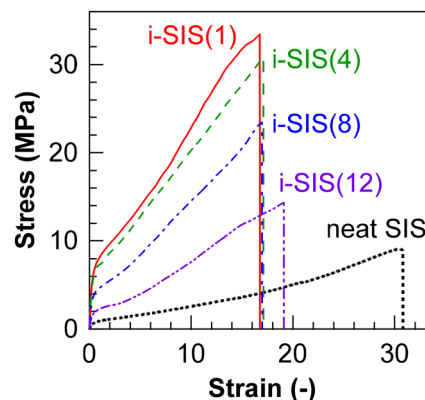
The values for E_Y, tensile strength (σ_{max}), elongation at break (ε_b), and W_T for neat SIS were 3.5 MPa, 9.0 MPa, 30, and 130 MJ m^{-3}, respectively (Table 1). The E_Y, σ_{max}, ε_b, and W_T values for i-SIS(12), which has the longest alkyl side chains, were 8.3 MPa, 14 MPa, 19, and 150 MJ m^{-3}, respectively. In other words, while the ε_b of i-SIS(12) was approximately 0.63 times that of neat SIS, the E_Y and σ_{max} of i-SIS(12) were 2.4 and 1.6 times higher than those of neat SIS, respectively. Consequently, the W_T of i-SIS(12) was also 1.2 times greater than that of neat SIS. As the alkyl side chain length shortened, ε_b slightly decreased, whereas E_Y and σ_{max} significantly increased, leading to a significant increase in W_T. Specifically, i-SIS(1), with the shortest alkyl side chain length, exhibited an ε_b of 16, which was 0.84 times that of i-SIS(12). In contrast, the E_Y and σ_{max} of i-SIS(1) were 32 MPa and 33 MPa, respectively, representing 3.9 times and 2.4 times higher values compared to i-SIS(12). Thus, the W_T of i-SIS(1) was also 320 MJ m^{-3}, which was 2.1 times greater than that of i-SIS(12). The higher E_Y and σ_{max} values of i-SIS(n) compared to neat SIS reflect the presence of the ionic aggregates, which act as physical cross-links within the rubber matrix of i-SIS(n). The ionic aggregates in i-SIS(n) with the shorter alkyl side chains exhibited large dimensions due to the easier approach among ion pairs, facilitated by the reduced steric hindrance associated with the shorter chain length. These larger ionic aggregates, composed of a greater number of ion pairs, generated strong ionic interactions, thereby acting as robust physical cross-links. Consequently, i-SIS(n) with the shorter alkyl side chains exhibited higher stress compared to i-SIS(n) with the longer alkyl side chains. Meanwhile, the ionic aggregates exhibited dynamic mechanical properties, characterized by stress dissipation effects. There effects are attributed to the repeated disassembly of the aggregates under applied forces and their reassembly upon the removal of the forces. The higher stress resulting from the shorter alkyl side chains in i-SIS(n) facilitated the easier pull-out of polymer chains from the polystyrene hard domains during elongation, leading to a reduced ε_b. On the other hand, the reduced steric hindrance associated

with the shorter alkyl chain length facilitated the easier approach among ion pairs, enabling more effective stress dissipation. This mechanism suppressed the pull-out of polymer chains from the polystyrene hard domains during elongation. As a result of these opposing effects, i-SIS(n) with the shorter alkyl side chain lengths did not break at small elongations, and its ε_b remained relatively unchanged.

4. Conclusions

In this study, we synthesized ionic thermoplastic elastomers, i-SIS(n), and investigated the effects of side alkyl chain length on the formation of ionic aggregates and their mechanical properties. The s-SIS containing 7.1 mol% of succinic anhydride units was synthesized from neat SIS. Subsequently, h-SIS(n), which contained carboxy groups, amide groups, and alkyl side chains with carbon numbers (n) of 1, 4, 8, and 12, was synthesized via acyl substitution reaction of normal alkylamine with the succinic anhydride units in s-SIS. The four i-SIS(n) samples with different alkyl side chain lengths were prepared by neutralizing the carboxyl groups in h-SIS(n) using sodium methoxide. TEM observations and SAXS measurements revealed that both neat SIS and all the i-SIS(n) films formed cylindrical structures. However, i-SIS(n) exhibited slightly smaller domain spacing and a less oriented periodic structure compared to neat SIS. SAXS measurements confirmed that the i-SIS(n) films formed microscopic ionic aggregates, with core dimensions of 1.1 nm for i-SIS(1) and 0.73 nm for i-SIS(12). The larger ionic aggregates in i-SIS(n) with shorter alkyl side chains, compared to those with longer alkyl side chains, were attributed to the easier approach among ion pairs, facilitated by the reduced steric hindrance associated with the shorter alkyl chain length.

Dynamic mechanical measurements revealed that i-SIS(n) exhibited a relaxation mode associated with the disassembly/re-assembly of the ionic aggregates. At room temperature, the tan δ curves of i-SIS(1) and i-SIS(12) showed peaks at 4.0×10^{-3} s^{-1} and 4.0×10^{0} s^{-1}, respectively. The presence of these peaks suggests that the relaxation mode associated with the ionic aggregates in i-SIS(n) with the shorter alkyl side chains is observed on a slower timescale compared to that in i-SIS(n) with longer alkyl side chains. Consequently, the ionic aggregates in i-SIS(n) with shorter alkyl side chains acted as robust physical cross-links. Due to the effects of the ionic aggregates as physical cross-links, i-SIS(n) demonstrated superior tensile properties compared to neat SIS. For instance, i-SIS(12) exhibited a σ_{max} that was 2.4 times higher and a W_T that was 1.2 times larger than those of neat SIS. Furthermore, the σ_{max} and W_T of i-SIS(1), which has the shortest alkyl side chains, were 2.4 and 2.1 times greater, respectively, than those of i-SIS(12). The excellent tensile properties of i-SIS(1) were attributed to the easiest approach among ion pairs, facilitated by the reduced steric hindrance associated with the shortest alkyl chain length, and the significant stress dissipation effects arising from the repeated disassembly and reassembly mecha-

nism of the ionic aggregates. In the future, we will investigate and report tensile properties of the polymers before ionization. We will also investigate thermal degradation properties, hydrophilic/hydrophobic nature, and the elastic recovery properties of i-SIS(n). i-SIS with shorter alkyl side chains was found to exhibit superior tensile properties compared to i-SIS with longer alkyl side chains. Additionally, our findings suggest that adjusting the alkyl side chain length enables the customization of various viscoelastic and tensile properties, making these ionic TPEs suitable for a wide range of applications across fields.

Author contributions

Kei Suzuki: data curation, investigation, writing-original draft. Takato Kajita: data curation, investigation, visualization, writing-original draft. Mako Ota: investigation. Yuki Nakama: investigation. Yuki Tamura: investigation. Saki Kinoshita: investigation. Daisuke Kato: resources. Ryoji Oda: conceptualization, resources. Sadaharu Hashimoto: conceptualization, resources. Atsushi Noro: conceptualization, funding acquisition, writing-review & editing, visualization, project administration, supervision.

Data availability

The data supporting this article have been included as part of the ESI.†
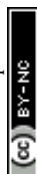
Conflicts of interest

The authors declare no competing interests.

Acknowledgements

References

1 F. S. Bates, M. A. Hillmyer, T. P. Lodge, C. M. Bates, K. T. Delaney and G. H. Fredrickson, *Science*, 2012, **336**, 434–440.
2 C. M. Bates and F. S. Bates, *Macromolecules*, 2017, **50**, 3–22.
3 G. Holden, *Thermoplastic elastomers*, Hanser Publishers, 1996.

4 W. Wang, W. Lu, A. Goodwin, H. Wang, P. Yin, N.-G. Kang, K. Hong and J. W. Mays, *Prog. Polym. Sci.*, 2019, **95**, 1–31.

5 H. Watanabe, *Macromolecules*, 1995, **28**, 5006–5011.

6 A. Takano, I. Kamaya, Y. Takahashi and Y. Matsushita, *Macromolecules*, 2005, **38**, 9718–9723.

7 J. M. Widin, A. K. Schmitt, A. L. Schmitt, K. Im and M. K. Mahanthappa, *J. Am. Chem. Soc.*, 2012, **134**, 3834–3844.

8 W. Shi, N. A. Lynd, D. Montarnal, Y. Luo, G. H. Fredrickson, E. J. Kramer, C. Ntaras, A. Avgeropoulos and A. Hexemer, *Macromolecules*, 2014, **47**, 2037–2043.

9 V. Hirschberg, M. G. Schußmann, M.-C. Röpert, N. Dingenouts, S. Buchheiser, H. Nirschl, J. Berson and M. Wilhelm, *Macromolecules*, 2024, **57**, 3387–3396.

10 M. Szwarc, *Nature*, 1956, **178**, 1168–1169.

11 M. Szwarc, M. Levy and R. Milkovich, *J. Am. Chem. Soc.*, 1956, **78**, 2656–2657.

12 G. Holden and R. Milkovich, *US Pat*, 3265765A, 1966.

13 J. T. Bailey, E. T. Bishop, W. R. Hendrick, G. Holden and N. R. Legge, *Rubber Age*, 1966, **98**, 69–74.

14 Thermoplastic Elastomers Market Size, Share & Trends Analysis Report By Application (Automotive, Industrial, Medical), By Material (Poly Styrenes, Poly Olefins), By Region, *And Segment Forecasts, 2024–2030, Grand View Research*, San Francisco, CA, 2024, ISBN: 978-1-68038-478-9.

15 R. P. Sijbesma, F. H. Beijer, L. Brunsveld, B. J. B. Folmer, J. H. K. K. Hirschberg, R. F. M. Lange, J. K. L. Lowe and E. W. Meijer, *Science*, 1997, **278**, 1601–1604.

16 K. Chino and M. Ashiura, *Macromolecules*, 2001, **34**, 9201–9204.

17 P. Cordier, F. Tournilhac, C. Soulié-Ziakovic and L. Leibler, *Nature*, 2008, **451**, 977–980.

18 A. Noro, Y. Matsushita and T. P. Lodge, *Macromolecules*, 2008, **41**, 5839–5844.

19 Y. Chen, A. M. Kushner, G. A. Williams and Z. Guan, *Nat. Chem.*, 2012, **4**, 467–472.

20 O. Altintas, E. Lejeune, P. Gerstel and C. Barner-Kowollik, *Polym. Chem.*, 2012, **3**, 640–651.

21 H. J. Zhang, T. L. Sun, A. K. Zhang, Y. Ikura, T. Nakajima, T. Nonoyama, T. Kurokawa, O. Ito, H. Ishitobi and J. P. Gong, *Adv. Mater.*, 2016, **28**, 4884–4890.

22 J.-X. Yang, Y.-Y. Long, L. Pan, Y.-F. Men and Y.-S. Li, *ACS Appl. Mater. Interfaces*, 2016, **8**, 12445–12455.

23 R. Tamate, K. Hashimoto, T. Horii, M. Hirasawa, X. Li, M. Shibayama and M. Watanabe, *Adv. Mater.*, 2018, **30**, 1802792.

24 K. G. Cho, S. An, D. H. Cho, J. H. Kim, J. Nam, M. Kim and K. H. Lee, *Adv. Funct. Mater.*, 2021, **31**, 2102386.

25 J. Choi, S. Kim, J. Yoo, S.-H. Choi and K. Char, *Macromolecules*, 2021, **54**, 6389–6399.

26 S. R. Petersen, H. Prydderch, J. C. Worch, C. J. Stubbs, Z. Wang, J. Yu, M. C. Arno, A. V. Dobrynin, M. L. Becker and A. P. Dove, *Angew. Chem., Int. Ed.*, 2022, **61**, e202115904.

27 G. R. Whittell, M. D. Hager, U. S. Schubert and I. Manners, *Nat. Mater.*, 2011, **10**, 176–188.

28 M. Burnworth, L. Tang, J. R. Kumpfer, A. J. Duncan, F. L. Beyer, G. L. Fiore, S. J. Rowan and C. Weder, *Nature*, 2011, **472**, 334.

29 H. Xu, J. Nishida, W. Ma, H. Wu, M. Kobayashi, H. Otsuka and A. Takahara, *ACS Macro Lett.*, 2012, **1**, 457–460.

30 A. Noro, S. Matsushima, X. He, M. Hayashi and Y. Matsushita, *Macromolecules*, 2013, **46**, 8304–8310.

31 T. Ueki, Y. Takasaki, K. Bundo, T. Ueno, T. Sakai, Y. Akagi and R. Yoshida, *Soft Matter*, 2014, **10**, 1349–1355.

32 Z. Tang, J. Huang, B. Guo, L. Zhang and F. Liu, *Macromolecules*, 2016, **49**, 1781–1789.

33 M. Yan, L. Cao, C. Xu and Y. Chen, *Macromolecules*, 2019, **52**, 4329–4340.

34 J. N. Hunt, K. E. Feldman, N. A. Lynd, J. Deek, L. M. Campos, J. M. Spruell, B. M. Hernandez, E. J. Kramer and C. J. Hawker, *Adv. Mater.*, 2011, **23**, 2327–2331.

35 T. L. Sun, T. Kurokawa, S. Kuroda, A. B. Ihsan, T. Akasaki, K. Sato, M. A. Haque, T. Nakajima and J. P. Gong, *Nat. Mater.*, 2013, **12**, 932–937.

36 K. Mayumi, A. Marcellan, G. Ducouret, C. Creton and T. Narita, *ACS Macro Lett.*, 2013, **2**, 1065–1068.

37 Y. Miwa, T. Kondo and S. Kutsumizu, *Macromolecules*, 2013, **46**, 5232–5237.

38 E. Filippidi, T. R. Cristiani, C. D. Eisenbach, J. H. Waite, J. N. Israelachvili, B. K. Ahn and M. T. Valentine, *Science*, 2017, **358**, 502–505.

39 Y. Miwa, J. Kurachi, Y. Kohbara and S. Kutsumizu, *Commun. Chem.*, 2018, **1**, 5.

40 D. Aoki, K. Yasuda and K. Arimitsu, *ACS Macro Lett.*, 2023, **12**, 462–467.

41 J. Zhang, X. Mao, Z. Ma, L. Pan, B. Wang and Y. Li, *Macromolecules*, 2023, **56**, 4219–4230.

42 Y. Okumura and K. Ito, *Adv. Mater.*, 2001, **13**, 485–487.

43 T. Oku, Y. Furusho and T. Takata, *Angew. Chem., Int. Ed.*, 2004, **43**, 966–969.

44 Y. Takashima, S. Hatanaka, M. Otsubo, M. Nakahata, T. Kakuta, A. Hashidzume, H. Yamaguchi and A. Harada, *Nat. Commun.*, 2012, **3**, 1270.

45 R. A. Weiss, A. Sen, C. L. Willis and L. A. Pottick, *Polymer*, 1991, **32**, 1867–1874.

46 B. D. Mather, M. B. Baker, F. L. Beyer, M. A. G. Berg, M. D. Greeny and T. E. Long, *Macromolecules*, 2007, **40**, 6834–6845.

47 M. Hayashi, S. Matsushima, A. Noro and Y. Matsushita, *Macromolecules*, 2015, **48**, 421–431.

48 T. Kajita, A. Noro and Y. Matsushita, *Polymer*, 2017, **128**, 297–310.

49 S. Yoshida, H. Ejima and N. Yoshie, *Adv. Funct. Mater.*, 2017, **27**, 1701670.

50 W. Ding and M. L. Robertson, *Eur. Polym. J.*, 2019, **113**, 411–423.

51 T. Kajita, H. Tanaka, A. Noro, Y. Matsushita, A. Nozawa, K. Isobe, R. Oda and S. Hashimoto, *Polymer*, 2021, **217**, 123419.

52 T. Kajita, A. Noro, R. Oda and S. Hashimoto, *ACS Omega*, 2022, **7**, 2821–2830.

53 K. Isobe, S. Hashimoto, A. Noro, T. Kajita, H. Tanaka and Y. Matsushita, *US Pat*, 11459417B2, 2022.

54 R. Longworth and D. J. Vaughan, *Nature*, 1968, **218**, 85–87.

55 A. Eisenberg, B. Hird and R. B. Moore, *Macromolecules*, 1990, **23**, 4098–4107.

56 K. I. Winey, *Science*, 2017, **358**, 449–450.

57 S. Yamada, T. Kajita, M. Nishimoto, J. Horiuchi, Y. Fujii, K. Sakaguchi, K. Hattori, H. Tamura, T. Kano, T. Sakai and A. Noro, *ACS Appl. Mater. Interfaces*, 2024, **16**, 65270–65280.

58 Y. Nagata, J. Masuda, A. Noro, D. Cho, A. Takano and Y. Matsushita, *Macromolecules*, 2005, **38**, 10220–10225.

59 A. Noro, A. Tamura, S. Wakao, A. Takano and Y. Matsushita, *Macromolecules*, 2008, **41**, 9277–9283.

60 D. J. Yarusso and S. L. Cooper, *Macromolecules*, 1983, **16**, 1871–1880.

61 D. J. Yarusso and S. L. Cooper, *Polymer*, 1985, **26**, 371–378.

62 Y. Miwa, Y. Kohbara, H. Furukawa and S. Kutsumizu, *Polymer*, 2018, **148**, 303–309.

63 D. J. Skrovanek, S. E. Howe, P. C. Painter and M. M. Coleman, *Macromolecules*, 1985, **18**, 1676–1683.

64 J. Dong, Y. Ozaki and K. Nakashima, *Macromolecules*, 1997, **30**, 1111–1117.

65 M. F. Tse, *J. Adhes. Sci. Technol.*, 1989, **3**, 551–570.

66 L. Andruzzi, E. Chiellini, G. Galli, X. Li, S. H. Kang and C. K. Ober, *J. Mater. Chem.*, 2002, **12**, 1684–1692.